EBSA
Biophysics in Europe

Predicting optoacoustic spectral behaviour of human erythrocytes, stomatocytes and echinocytes using a modified Green's function method

Ratan K. Saha[1]

Abstract

Optoacoustic (OA) spectral properties of various sources mimicking normal and pathological red blood cells (RBCs) have been studied. The shapes of normal RBC and cells suffering from stomatocytosis (denoted by ST) were generated using mathematical models. However, the shape corresponding to the cells affected by echinocytosis (referred to as ET) was constructed by uniformly distributing half prolate spheroids on a central spherical object. The OA field emitted by an acoustically inhomogeneous source was calculated for a wide acoustic frequency bandwidth (1–1500 MHz with an increment 5 MHz) by solving the time-independent wave equation employing a modified Green's function approach. The OA spectra averaged over 200 orientations for normal RBC and STs demonstrate similar features (one minimum occurring nearly at 906 MHz). The same graphs for ETs are remarkably different from that of normal RBC and exhibit better match with that of a spherical RBC (first minimum appearing at around 425 MHz). The spectral features of ETs above 425 MHz may enable us to differentiate diseased cells (echinocytosis) from normal RBCs.

Keywords Optoacoustics · Photoacoustics · Inhomogeneous wave equation · Green's function · Modified Green's function · Normal erythrocyte · Stomatocyte · Echinocyte

Introduction

In 1880, Alexander Graham Bell discovered the optoacoustic/photoacoustic (OA/PA) effect—-generation of acoustic waves due to absorption of light (Wang 2017). It has attracted tremendous attention over the last three decades because it has the potential to evolve as a biomedical imaging/characterization modality (Wang and Yao 2016; Das et al. 2021). It combines the advantages of optics and acoustics. The OA tomography technology can generate images of small animal organs. The OA microscopy technique can provide images of cells, narrow vasculatures, etc. Apart from imaging studies, the OA signals from circulating tumor cells and malaria infected cells in blood stream have been captured using transducers operating at 2.25–35 MHz (Galanzha et al. 2013; Juratli et al. 2016). The OA signals from single red blood cells (RBCs) have also been measured using ultra high frequency transducers (few hundred MHz to GHz) and subsequently, spectral features have been studied (Strohm et al. 2013a, b). It has been concluded that spectral patterns depend upon the size and shape of RBCs. In other words, the morphological parameters of the OA source may be extracted from the frequency domain properties.

It is worthy to mention here that RBCs under normal physiological condition retain the biconcave shape (Bessis 1973; Da Costa et al. 2013; He Li et al. 2018; Gerald Lim et al. 2002). The surface to volume ratio for this shape is very high. Further, RBCs do not have nucleus and hence they are astonishingly deformable allowing them to travel through microchannels (whose diameters are less than the diameter of a typical RBC). High surface to volume ratio and deformability are the two unique features of RBCs which help them to perform physiological activities efficiently. Some hereditary disorders make RBCs stiff and deformed inhibiting their regular functions to perform. Stomatocytosis (ST) and echinocytosis (ET) are such disorders. In case of ST, RBCs take cup shape. In case of ET, RBCs appear

✉ Ratan K. Saha
ratank.saha@iiita.ac.in

1 Department of Applied Sciences, Indian Institute of Information Technology Allahabad, Jhalwa, Allahabad 211015, India

as crenated shapes. These shapes are further divided into three classes referred to as I, II and III. Several protuberances/spicules (number varying from 20 to 50) are found to be uniformly distributed on a central spherical body in ET III (Ranjan Mukhopadhyay et al. 2002). Understanding of these shapes and how they transform have served as a classic problem in cell biology (Ranjan Mukhopadhyay et al. 2002). Detection and classification of abnormal RBCs are also of great clinical importance. The OA technique may be developed for fast and automated characterization of pathological RBCs.

The OA fields for normal and altered RBCs have been calculated by solving the Helmholtz equation numerically via the Green's function method (Saha et al. 2017; Kaushik et al. 2019). Further, the size and shape information of the source have also been extracted from the OA spectrum (Kaushik et al. 2020, 2021). In these studies, RBCs are assumed to be acoustically homogeneous with respect to the ambient medium. However, this assumption is not true because sound-speed inside RBCs differs from that of saline water by $\approx 10\%$. The term arising from sound-speed mismatch (between the source and the ambient medium) can be easily incorporated within the Helmholtz equation. Nevertheless, it is not trivial to obtain a solution to that equation. The Born series methods have been implemented to solve such an equation (Kaushik et al. 2020; Saha 2020). The traditional Born series method can provide converging solution when size of the source and sound-speed mismatch are small. The convergent Born series technique can work faithfully for arbitrarily large media. The Born series methods are computationally expensive and that is why recently a modified Green's function method has been utilized to solve the OA wave equation for an acoustically inhomogeneous source (Saha 2021). The performance of this scheme has been extensively investigated (Saha 2021).

The objective of this work is to study the OA spectra generated by various acoustically inhomogeneous objects lying in the cellular regime when computed employing the modified Green's function method. This approach provides an integral solution to the OA wave equation. The Monte Carlo method was employed to compute the integration numerically to evaluate frequency dependent pressure fields emitted by a series of OA sources imitating biological targets (i.e., human erythrocytes, STs and ETs). The contours of erythrocytes and STs were generated using mathematical equations whereas a shape mimicking ET was constructed by placing half prolate spheroids on the surface of a sphere. The OA spectra averaged over 200 orientations for erythrocytes and STs look identical but those of ETs appear significantly different. These findings suggest that OA technique may be explored for differentiating ETs from normal RBC.

The layout of the paper is as follows. In the next section, we describe how to solve the time-independent OA equation

using the modified Green's function method and illustrate the mathematical models to simulate the shapes for a series of cells (normal and pathological RBCs). The construction of shapes of these cells and computation of OA spectra are detailed in section 3. The simulation results are presented in section 4. Various aspects of this study are elaborated in section 5. This section also includes a brief summary of the work.

Governing equations

OA wave equation and its solution

Consider an optically transparent fluid medium enclosing a light absorbing region, which is uniformly illuminated by a laser beam. Thermo-opto-mechanical properties of this region are spatially invariant. The sound-speed of this region differs from that of the surrounding medium. The corresponding time-independent OA wave equation under thermal and stress confinement conditions is given by (Diebold et al. 1991),

$$\nabla^2 \psi(\mathbf{r}) + k_s^2 \psi(\mathbf{r}) = \frac{i\mu\beta I_0 \omega}{C_P}, \quad \text{within the source,} \quad (1a)$$

$$\nabla^2 \psi(\mathbf{r}) + k_f^2 \psi(\mathbf{r}) = 0, \quad \text{in the surrounding medium,} \quad (1b)$$

where μ is the optical absorption coefficient, β indicates the isobaric thermal expansion coefficient and C_P specifies the specific heat for the absorbing region; Here, k_s and k_f refer to the wave numbers inside and outside the OA source, respectively. The notations ω and I_0 are used to denote the modulation frequency and the intensity of the incident laser beam, respectively. Fig. 1 displays a representative diagram in 2D.

The OA wave equations as given in Eq. (1) after rearrangement of terms can be combined as (Kaushik et al. 2020; Saha 2020, 2021),

$$\nabla^2 \psi(\mathbf{r}) + k_f^2 \psi(\mathbf{r}) = -S(\mathbf{r}) - V(\mathbf{r})\psi(\mathbf{r}), \quad (2)$$
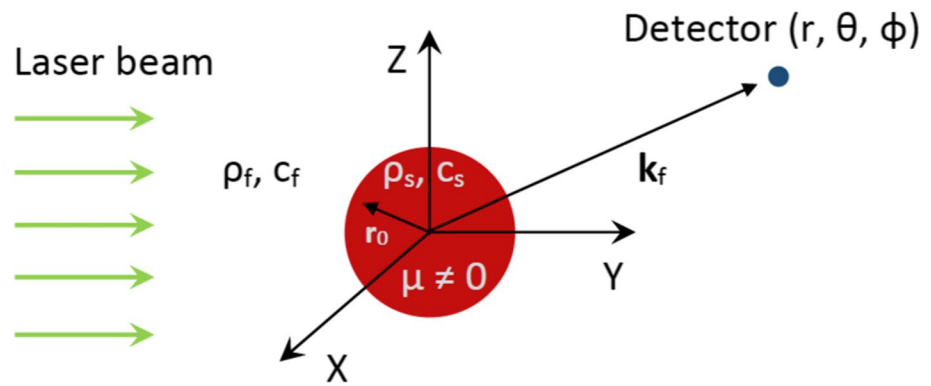
where

$$S(\mathbf{r}) = \begin{cases} -\frac{i\mu\beta I_o \omega}{C_p}, & \text{if } |\mathbf{r}| \leq a \\ 0, & \text{if } |\mathbf{r}| > a \end{cases} \quad (3)$$

and

$$V(\mathbf{r}) = \begin{cases} k_s^2 - k_f^2, & \text{if } |\mathbf{r}| \leq a \\ 0, & \text{if } |\mathbf{r}| > a, \end{cases} \quad (4)$$

where $S(\mathbf{r})$ and $V(\mathbf{r})$ denote the source term and the scattering potential, respectively. Here, we consider a spherical

Fig. 1 2D view of the source–detector arrangement.

source with radius a. Similar equations frequently appear in physics modeling acoustical, optical and potential scattering problems (Philip 1968; Ishimaru 2002; Leonard 1969). These equations can be solved using the perturbation method (Leonard 1969). This method obtains an approximate solution of a complex equation starting from a simple/known solution. This procedure provides sufficient insight about how the system depends upon various parameters.

The solution to Eq. (2) can also be obtained using the Green's function method. Note that the free space Green's function satisfies (Morse and Feshbach 1953),

$$\nabla^2 g(\mathbf{r}|\mathbf{r}_0) + k_f^2 g(\mathbf{r}|\mathbf{r}_0) = -\delta(\mathbf{r} - \mathbf{r}_0),\qquad(5)$$

where δ indicates the Dirac delta function; $\mathbf{r}_0$ and $\mathbf{r}$ are the source and the field points, respectively. The functional form of $g(\mathbf{r}|\mathbf{r}_0)$ can be derived as (Morse and Feshbach 1953),

$$g(\mathbf{r}|\mathbf{r}_0) = \frac{e^{ik_f|\mathbf{r}-\mathbf{r}_0|}}{4\pi|\mathbf{r}-\mathbf{r}_0|}.\qquad(6)$$

The solution to Eq. (2), thus, becomes,

$$\psi(\mathbf{r}) = \int_{V_{vol}} g(\mathbf{r}|\mathbf{r}_0)[S(\mathbf{r}_0) + V(\mathbf{r}_0)\psi(\mathbf{r}_0)]d^3\mathbf{r}_0,\qquad(7)$$

where V_{vol} is the volume of the source. Deriving a solution $\psi(\mathbf{r})$ is not trivial as evident from Eq. (7). This is because the field inside the source has to be given as an input to Eq. (7) to obtain the pressure field outside the OA source. In reality, it is not known *a priori*. The standard procedure is to begin with an approximate field and a reliable solution is obtained by recursively expanding Eq. (7). This is known as the Born series method (Kaushik et al. 2020; Saha 2020, 2021). Though the Born series methods work well for acoustically inhomogeneous source but they are computationally expensive.

It has been recently shown that a reliable estimate of the OA field for an acoustically inhomogeneous source can be deduced by only considering the first source term (neglecting the scattering potential) and by modifying the

free space Green's function (in the far field) in the following manner (Saha 2021; Chu and Ye 1999),

$$g(\mathbf{r}|\mathbf{r}_0) \approx \frac{e^{ik_f r}}{4\pi r}e^{-i\mathbf{k}_s\cdot\mathbf{r}_0}.\qquad(8)$$

Chu et al. utilized this modified Green's function in the context of underwater acoustics for studying scattering of acoustic waves by Zooplankton (Chu and Ye 1999). The acoustical property of the inhomogeneity is included within the Green's function in this scheme and thus can efficiently compensate the phase mismatch arising due to sound-speed mismatch facilitating accurate estimation of backscatter spectrum (Chu and Ye 1999; Sharma and Saha 2009). Therefore, for this Green's function, one calculates,

$$\begin{aligned}\psi_{mgf}(\mathbf{r}) &\approx -\int_{V_{vol}} \frac{i\mu\beta I_o\omega}{C_p}\frac{e^{ik_f r}}{4\pi r}e^{-i\mathbf{k}_s\cdot\mathbf{r}_0}d^3\mathbf{r}_0,\\ &= M(\mathbf{k})\frac{e^{ik_f r}}{r},\end{aligned}\qquad(9)$$

where $M(\mathbf{k})$ is the amplitude of the out going spherical wave and it is given by,

$$M(\mathbf{k}) = -\int_{V_{vol}} \frac{i\mu\beta I_o\omega}{4\pi C_p}e^{-i\mathbf{k}_s\cdot\mathbf{r}_0}d^3\mathbf{r}_0.\qquad(10)$$
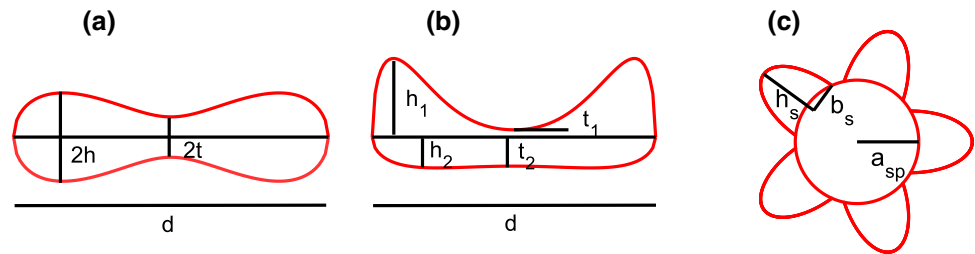
For a spherical source, one finds,

$$\psi_{mgf}(\mathbf{r}) = -\frac{i\mu\beta I_o\omega a^3}{C_p}\frac{[\sin(k_s a) - k_s a\cos(k_s a)]}{k_s^3 a^3}\frac{e^{ik_f r}}{r}.\qquad(11)$$

In this work, Eq. (10) has been computed to predict the OA fields generated by normal and pathological RBCs.

It may be mentioned here that the exact analytical solutions of Eq. (1) can be readily derived for regular shapes (e.g., layer, infinite cylinder, sphere). It is accomplished by solving these equations inside and outside the source and then by matching the pressure and normal component of the particle velocity at the boundary. For example, the solution for a spherical source becomes,

$$\psi_{ex}(\mathbf{r})$$

$$= \frac{i\mu\beta I_0 \omega a^3}{C_P} \frac{[\sin(\hat{q}) - \hat{q}\cos(\hat{q})]}{\hat{q}^3[(1-\hat{\rho})\sin(\hat{q})/\hat{q} - \cos(\hat{q}) + i\hat{\rho}\hat{v}\sin(\hat{q})]} \frac{e^{ik_f(r-a)}}{r},$$

$$(12)$$

where $\hat{q} = k_s a$, $\hat{v} = v_s/v_f$ and $\hat{\rho} = \rho_s/\rho_f$; ρ_s and v_s are the density and sound-speed inside the source, respectively. The same quantities for the ambient fluid medium are denoted by ρ_f and v_f, respectively. Eq. (12) has also been evaluated in this work to compare the performance of the modified Green's function approach. Note that the Green's function method approximately reproduces (apart from some phase factors) the exact solution for a spherical source [compare Eqs. (11) and (12)].

Modeling of shapes of normal and pathological cells

Muñoz San Martín et al. developed parametric equations using the Jacobi elliptic functions that can suitably model various shapes of normal and pathological RBCs (belonging to ST) of constant volume (Muñoz San Martín et al. 2006). These equations are capable to produce continuous deformations from the normal to the altered shapes. However, the notations and also the equations are not easy to understand. Therefore, the corresponding equations in the Cartesian coordinate system were derived subsequently (Larkin and Kuchel 2010). This group also proposed a simple method for generating the shapes belonging to ET mathematically. The models are described below in brief.

Modeling of normal RBC

Equation for normal RBC can be given by, Larkin and Kuchel (2010)

$$(x^2 + y^2)^2 + A(x^2 + y^2) + Bz^2 + C = 0, \quad (13)$$

where x, y and z are lying on the surface of RBC. The coefficients A, B, C can be obtained as,

$$A = (1 - 2m)d^2/4m,$$
$$B = (1 - m)d^4/16t^2m,$$
$$C = -(1 - m)d^4/16m,$$

where d and $2t$ are the diameter and dimple thickness of the RBC, respectively; the parameter $m \in [0, 1]$ controls the maximum thickness of the cell. A schematic diagram is shown in Fig. 2a.

Modeling of ST

Unlike normal RBC, two equations are required to describe the contours of STs. These equations are given below,

$$(x^2 + y^2)^4 + D(x^2 + y^2)^3 + E(x^2 + y^2)^2 + F(x^2 + y^2) + Gz^2 + H = 0, \quad \text{upper half}, \quad (14a)$$

$$(x^2 + y^2)^3 + I(x^2 + y^2)^2 + J(x^2 + y^2) + Kz^2 + L = 0, \quad \text{lower half}. \quad (14b)$$

The coefficients D, E, F, G and H are related to the morphological parameters as,

$$D = -(4m_1 - 3)d^2/4m_1,$$
$$E = 3(1 - 3m_1 + 2m_1^2)d^4/16m_1^2,$$
$$F = -(m_1 - 1)^2(4m_1 - 1)d^6/64m_1^3,$$
$$G = (1 - m_1)^3 d^8/256t_1^2 m_1^3,$$
$$H = (m_1 - 1)^3 d^8/256m_1^3.$$

Similarly, the coefficients I, J, K and L can be found to be,

$$I = -(3m_2 - 2)d^2/4m_2,$$
$$J = (1 - 4m_2 + 3m_2^2)d^4/16m_2^2,$$
$$K = (1 - m_2)^2 d^6/64t_2^2 m_2^2,$$
$$L = -(m_2 - 1)^2 d^6/64m_2^2.$$

The maximum heights of the cell in the two halves are governed by the magnitudes of m_1 and m_2, respectively. A 2D plot of a ST shape generated by Eq. (14) is presented in Fig. 2b.

Modeling of ET

It is not possible to provide an analytical formula for modeling the ET shape. A simple approach involves placing of

Table 1 Numerical values of morphological parameters of different cells considered in this study (N_s represents the number of spicules)

Cell	Morphological parameters	Volume (μm^3)
Normal RBC	d = 7.8 μm, 2t = 1.0 μm, 2h = 2.19 μm, m = 0.9447	85.1
ST1	d = 7.8 μm, t_1 = 0.30 μm, m_1 = 0.80, t_2 = 0.70 μm, m_2 = 0.70	85.5
ST2	d = 7.8 μm, t_1 = 0.16 μm, m_1 = 0.885, t_2 = 0.84 μm, m_2 = 0.55	85.7
ST3	d = 7.8 μm, t_1 = 0.05 μm, m_1 = 0.9490, t_2 = 0.95 μm, m_2 = 0.4720	85.1
ET1	N_s = 20, a_{sp} = 2.70 μm, h_s = 0.41 μm, b_s = 0.4 μm	85.05
ET2	N_s = 20, a_{sp} = 2.62 μm, h_s = 1.0 μm, b_s = 0.5 μm	85.43
ET3	N_s = 20, a_{sp} = 2.49 μm, h_s = 2.0 μm, b_s = 0.5 μm	85.21
ET4	N_s = 31, a_{sp} = 2.69 μm, h_s = 0.41 μm, b_s = 0.4 μm	85.56
ET5	N_s = 31, a_{sp} = 2.55 μm, h_s = 1.0 μm, b_s = 0.5 μm	85.08
ET6	N_s = 31, a_{sp} = 2.34 μm, h_s = 2.0 μm, b_s = 0.5 μm	85.47
ET7	N_s = 40, a_{sp} = 2.67 μm, h_s = 0.41 μm, b_s = 0.4 μm	84.92
ET8	N_s = 40, a_{sp} = 2.50 μm, h_s = 1.0 μm, b_s = 0.5 μm	85.60
ET9	N_s = 40, a_{sp} = 2.20 μm, h_s = 2.0 μm, b_s = 0.5 μm	85.58

half prolate spheroids mimicking spicules uniformly on a sphere (Larkin and Kuchel 2010). Fig. 2c illustrates such a scenario in 2D. The equation of a spicule placed on a sphere at an angular location (ζ and ξ) is given by,

$$\frac{[(x\cos\xi + y\sin\xi)\cos\zeta - z\sin\zeta]^2}{b_s^2} + \frac{[x\sin\xi - y\cos\xi]^2}{b_s^2} +$$
$$\frac{[(x\cos\xi + y\sin\xi)\sin\zeta + z\cos\zeta - (a_{sp}^2 - b_s^2)^{\frac{1}{2}}]^2}{h_s^2} = 1,$$

(15)

where h_s and b_s are the lengths of the semi-axes of the prolate spheroid, respectively; a_{sp} is the radius of the inner sphere (see Fig. 2c). It may be emphasized that appropriate amount of rotations and a translation are given to the prolate spheroid so as to place its major axis perpendicular to the tangential plane (centered at ζ and ξ) of the inner sphere.

## Simulation method

Numerical construction of RBC shapes

The contour of the normal RBC was generated by evaluating Eq. (13). The numerical values of morphological parameters were taken from the literature (Muñoz San Martín et al. 2006; Larkin and Kuchel 2010) and are also given in Table 1 (second row). Accordingly, the coefficients A, B and C were calculated. Surface plot of normal RBC is demonstrated in Fig. 3a. The ST shape was formed by utilizing Eq. (14). As in the previous case, numerical values of various shape parameters were fixed on the basis of earlier works (Muñoz San Martín et al. 2006; Larkin and Kuchel 2010). Small variations in the shape parameters were also introduced to

produce three variants of ST (see rows 3 to 5 of Table 1). The corresponding plots are shown in Fig. 3b–d. All these cells nearly have the same volume.

The ET cells were formed *in silico* in the following way. At first angular positions (a set of ζ, ξ) of equispaced points (N_s) on the surface of a sphere of radius a_{sp} were identified (sivu https://www.cmu.edu/biolphys/deserno/pdf/sphere_equi.pdf). The coordinates of some points (i.e., x, y, z) on the surface of a half prolate spheroid (major axis along the z-axis) were generated. These points were rotated (counter clockwise) by an angle ζ with respect to the y-axis. Another rotation of ξ angle was given with respect to the z-axis. After that all the points were shifted linearly by $\sqrt{a_{sp}^2 - b_s^2}\sin\zeta\cos\xi$, $\sqrt{a_{sp}^2 - b_s^2}\sin\zeta\sin\xi$ and $\sqrt{a_{sp}^2 - b_s^2}\cos\zeta$ along the x, y and z directions. These two successive rotations and a linear translation positioned the prolate spheroid at the angular location of (ζ, ξ) on the top of the inner sphere. Furthermore, the prolate spheroid aligned perpendicular to the spherical surface at (ζ, ξ). Other spicules were placed at the desired locations by following the identical steps.

Table 1 (rows 6–14) details the numerical values of various parameters (N_s being the number of spicules). It has been seen that approximately 25–50 spicules typically cover the central spherical body in case of ET III. Furthermore, aspect ratio (spicule height over width at the base) is generally of the order of 0.8 (Ranjan Mukhopadhyay et al. 2002). In this study, the number of spicules was varied from 20 to 40. The radius of the inner sphere is consistent with the literature (Ranjan Mukhopadhyay et al. 2002). The numerical values of height and width of the base of the spicules were arbitrarily chosen making the aspect ratio on the higher side. Figures 3e–g display representative ET shapes of constant volume with $N_s = 20$.

Fig. 3 **a** Surface plot of normal RBC. **b–d** Same plots for the stomatocyte shapes. **e–g** 3D plots for the echinocyte shapes with number of spicules, $N_s = 20$. Spicule size increases gradually from **e–g**. Normal and deformed cells approximately have the same volume.
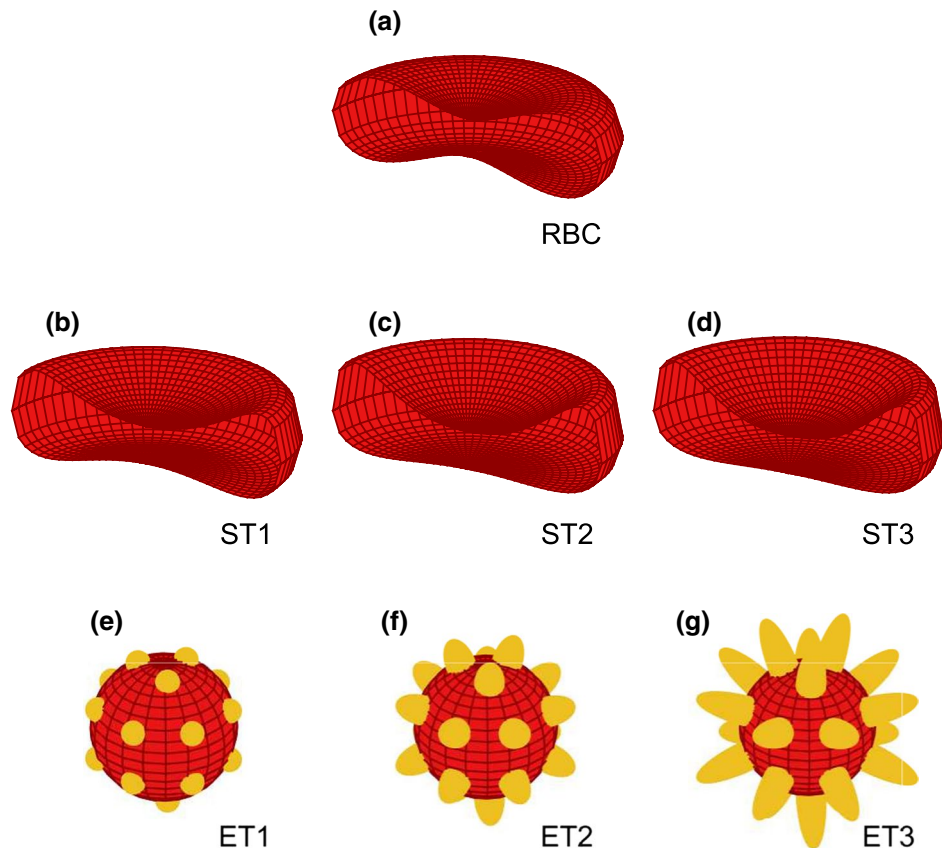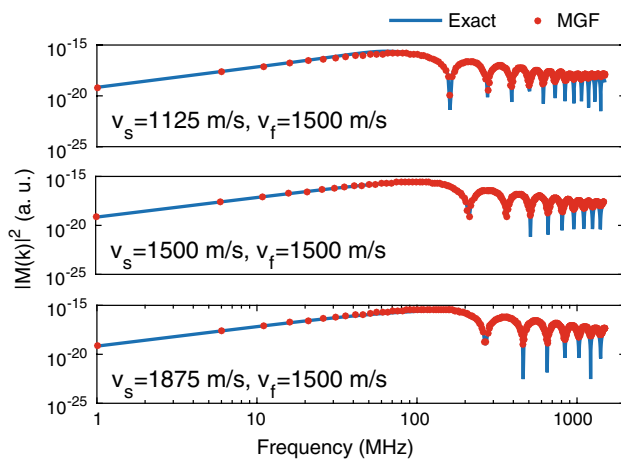

Computation of OA spectra

The amplitudes of the outgoing spherical waves for various source objects mimicking cells were evaluated by calculating Eq. (10) over a frequency range of 1–1500 MHz with a step size of 5 MHz. Single-cell OA experiments have been carried out in the GHz range and that is why the upper limit of the frequency band was fixed to 1.5 GHz. The numerical values of the thermo-opto-mechanical parameters were chosen as unity (i.e., $\mu = 1, \beta = 1, C_P = 1, I_0 = 1$). The magnitudes of these parameters control the strength of the OA field but the spectral features remain unaltered. At the first step, we computed the OA spectra for a spherical source with $a = 5 \ \mu$m as the radius using the modified Green's function approach. Subsequently, we compared the numerical results provided by this method and those of the exact technique. The sound speed inside the source was varied from $v_s = 1125$ to 1875 m/s. The same quantity outside the source was taken as $v_f = 1500$ m/s (i.e., sound-speed in saline water at 27° C) (Saha and Kolios 2011). Therefore, the sound-speed mismatch was about ±25%. In the second case, we obtained the OA spectra for normal and pathological RBCs. The sound-speed within the RBC was fixed at $v_s = 1639$ m/s. It corresponds to the actual value of sound-speed for RBC (Saha and Kolios 2011).

The Monte Carlo integration method was implemented to carry out the integration in Eq. (10). Essentially, a large number of points were randomly thrown inside a box. A cell of interest was placed at the center of this box. The OA fields for a particular frequency and at a specific detector location were calculated for the random points which lied inside the cell. These fields were summed up to obtain the OA spectrum. These steps were repeated for 200 detector locations (randomly positioned over the 4π angle) and the corresponding power spectra were added up to obtain the resultant spectrum averaged over 200 orientations. For example, a box of size $12 \times 12 \times 12 \ \mu$m³ was considered to bound a spherical source of radius $a = 5 \ \mu$m. Approximately, 500000 points were thrown within this box and more than 150000 points were found to be lied inside the sphere. A numerical code (in MATLAB 2015a) was written for this purpose and was executed in a personal computer (Windows 10 as the operating system, Intel(R) Core(TM) i3-6006U processor, 2.00 GHz clock speed, 8 GB RAM). It took less than 10 min to run for 200 orientations. Similarly, for normal RBC and STs, 500000 points were thrown inside a box of $8 \times 8 \times 4 \ \mu$m³ and out of which about 165000
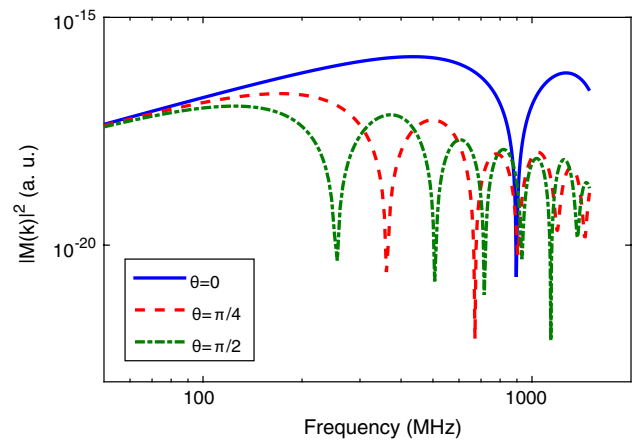
Fig. 4 Demonstration of the OA spectra computed for a spherical source (radius = 5 μm) under different sound-speed mismatch conditions (solid line for the exact method and dots for the modified Green's function (MGF) technique). Sound-speed inside the source is $v_s = 1125$ m/s in the top panel, $v_s = 1500$ m/s in the middle panel and $v_s = 1875$ m/s in the bottom panel; in all the cases, sound speed outside the source is $v_f = 1500$ m/s.

points occupied the source volume. For ETs, 1000000 random points were generated inside a box of $10 \times 10 \times 10 \mu$ m^3. Nearly, 210000 points (average) contributed to the field calculation and average execution time was about 13 min for 200 orientations. These Monte Carlo steps were sufficient enough to provide converging results for all the cases (comparable results were also obtained even when the Monte Carlo steps were doubled).

Simulation results

Plots of the OA spectra generated by a spherical source with radius $a = 5 \mu$m are shown in Fig. 4. The sound-speed inside the source is gradually increased from $v_s = 1125$ to 1875 m/s (from top to bottom). A similar spectrum for the exact analytical method is also included in each figure for comparison. Each spectrum exhibits well-known peaks and dips pattern which arises because of the spherical Bessel function (first kind and of order unity). It can be seen that the calculated spectra for the proposed scheme demonstrate perfect match with those of the exact method. Moreover, the first minimum shifts at higher frequency as the sound speed inside the source increases. This is expected because the width of the N-shape pulse (in the time domain) decreases as the sound-speed inside the source increases. As a result of that, first minimum shifts at a higher frequency. Figure 4 validates the approach presented herein for solving the OA wave equation in the frequency domain for acoustically inhomogeneous source.


Fig. 5 Illustration of the OA spectra for a normal RBC computed at three specific angles.

Figure 5 shows that the OA spectrum for a normal RBC passes through several maxima-minina (e.g., minima locations are at 256, 506, 716, 931, 1141, 1376 MHz) within the frequency bandwidth (1–1500 MHz) when the probing angle is $\theta = \pi/2$ (i.e., along the X/Y axis, see Fig. 1). Further, only one minimum occurs at 896 MHz when the field is computed along the axis of symmetry (i.e., $\theta = 0$, along the Z axis, see Fig. 1). The number of frequency minima gradually increases if the detector is moved from the Z direction to the X/Y direction as can be seen from this figure.

Simulated OA spectrum averaged over 200 orientations for a normal RBC is shown in Fig. 6a. The curve is plotted over a bandwidth of 50–1500 MHz to improve the clarity of the figure. The same plot for a spherical RBC is also presented in this figure for comparison. These two spectra appear comparable up to 266 MHz but after that they are remarkably different. The OA spectrum for a normal RBC in general exhibits an oscillatory pattern [see Fig. 5]. However, only one prominent dip is visible at nearly 906 MHz in this case owing to the orientation averaging. The OA spectrum for a spherical RBC contains several maxima and minima. The first dip appears at about 425 MHz which is much earlier than that of a normal RBC. The OA spectra for STs are drawn in Fig. 6b. These graphs are almost indistinguishable and also look identical to that of a normal RBC.

Similar plots for ETs are displayed in Fig. 7. Three separate figures are used to increase the visibility of each figure as well as to show small changes in each spectrum. The OA spectrum for ET1 appears as that of a sphere. This is obvious because the heights of the spicules are small in this case. It can be seen that the prominent peaks and dips pattern vanishes approximately above 575 MHz for ET2. It is also true for ET3. It may happen because OA fields from the protrusions, in addition to the inner spherical body, contribute in these cases and thus the spectra become relatively

Fig. 6 **a** Plots of the OA spectra averaged over 200 orientations (denoted by < − >) for normal and spherical RBCs. **b** Same as (**a**) but for the STs.
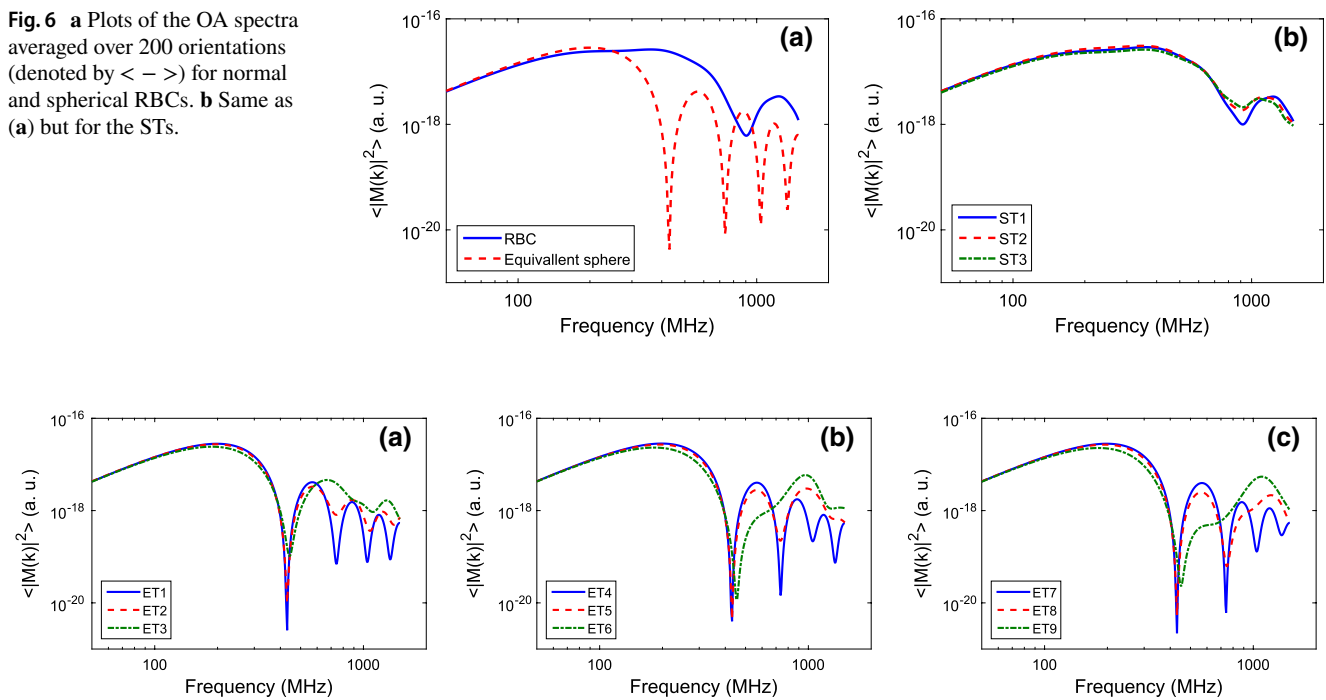
Fig. 7 **a**–**c** Demonstration of the OA spectra averaged over 200 orientations (indicated by < − >) for different variants of ETs.

flat. Similar observations can be made from Figs. 7b and c. However, an additional peak appears around 1000 MHz for ET6 and ET9.

Discussion and conclusions

Time-independent inhomogeneous OA wave equation is solved using a modified Green's function approach. In this formulation, acoustic property of the source is incorporated within the Green's function to appropriately model wave propagation inside the source. The calculated fields for this scheme demonstrate perfect match with those of the exact method. However, it has been seen that $M(\mathbf{k})$ is essentially calculated to be real (thus, does not have any imaginary part). Therefore, phase part of the OA field is not correctly reproduced in this method. Further, OA field calculation is accomplished by considering the first source term only (ignoring the scattering potential). It would be interesting in future to examine the validity of this method for calculating the OA field from a collection of acoustically inhomogeneous sources where multiple scattering of acoustic waves may take place because of nonvanishing scattering potentials.

In this work, it has been assumed that the PA source is uniformly irradiated by the incident laser beam. It may hold if the beam diameter is large compared to the characteristic dimensions of the source. However, for narrow beam (with respect to the source), it may not hold. Therefore, in future,

it would be interesting to examine the effect of gradient absorption profile on the OA spectrum. In addition to that, scattering (which is dependent on the shape of the source) and polarization of the incident light beam need to be incorporated within the model. Further studies are required to investigate these issues.

This work includes mathematical equations for generating contours of normal erythrocyte and STs. The framework is flexible enough so that continuous deformation from healthy erythrocyte to various variants of STs are possible. However, for ET shapes, such equations do not exist. Hence, a simple approach has been adopted here. It models each spicule as a half prolate spheroid and such spheroids have been uniformly placed on the surface of a sphere. It may be noted that in this approach ET shapes are described using only three parameters [radius of the inner sphere, height and width (at the base) of the spicules]. Nevertheless, there exists a drawback in this modeling approach. In fact, junctions between the spicules and the spherical object are not continuous curves unlike real ET shapes (Larkin and Kuchel 2010). An attempt may be made to generate ET structures using spherical harmonic expansions so that the junctions would become smooth and continuous.

The PA spectra for a normal RBC contain several maxima and minima [see Fig. 5]; however, the spectrum shown in Fig. 6a looks relatively flat (only one minimum occurs at 906 MHz). This is also true for STs (see Fig. 6b). This is because of the orientation averaging. However, the

fluctuations are greatly vivid in Fig. 6a for the spherical RBC. Similar observations can also be made from Fig. 7. Moreover, each spectrum gets affected by the spicules after the first minimum (approximately 430 MHz). In this study, we considered 200 orientations of the target particle while computing the average spectrum. The morphological parameters of the test object can then be obtained from such an averaged PA spectrum by utilizing an inverse problem framework (Kaushik et al. 2020). In a typical experimental situation, few hundred cells are examined (Neukammer et al. 2003) and these cells may have different orientations when they encounter the incident laser beam (see bottom row of Fig. 1 of Kaushik et al. 2020). Therefore, the effect of orientation averaging is always embedded in an experimentally obtained average spectrum. The simulation of PA spectrum averaged over many orientations better emulates the experimental situation.

Recently, we computed OA spectra for a series of acoustically homogeneous sources resembling cells (Kaushik et al. 2020). This procedure included various realistic factors such as detector with finite aperture, acoustically lossy and dispersive coupling medium (from source to detector) and intra-variability of the source while estimating the spectrum. We also presented an inverse problem framework for obtaining the size and shape information of the source from the OA spectrum using form factor models (Kaushik et al. 2020). We speculate that this analysis protocol may find applications for analyzing OA flow cytometry data (Strohm et al. 2013a, b). Therefore, in future, it would be interesting to utilize this spectrum analysis methodology for analyzing the spectra generated by acoustically inhomogeneous source (as presented in this work) for simultaneous characterization of source morphology and speed of sound inside the source.

In conclusion, the time-independent OA wave equation for an acoustically inhomogeneous source (with respect to the ambient medium) is solved deploying a modified Green's function method. In this approach, acoustic property of the source is incorporated while modeling the wave propagation inside the source. This strategy works very well for acoustically inhomogeneous source and emerges out as a very fast and accurate method. This framework has been utilized to compute the OA spectra for normal RBC and cells affected by stomatocytosis and echinocytosis. The OA spectra averaged over many orientations for ETs are significantly different from those of normal RBC and STs. Therefore, detection of cells suffering from echinocytosis from normal RBCs may be feasible and finally, this observation may help to develop an OA technology for cell characterization.

References

Bessis Marcel (1973) Red cell shapes. An illustrated classification and its rationale. Springer, Berlin, pp 1–25

Chu Dezhang, Ye Zhen (1999) A phase-compensated distorted wave born approximation representation of the bistatic scattering by weakly scattering objects: Application to zooplankton. J Acoust Soc Am 106(4):1732–1743

Da Costa Lydie, Galimand Julie, Fenneteau Odile, Mohandas Narla (2013) Hereditary spherocytosis, elliptocytosis, and other red cell membrane disorders. Blood Rev 27(4):167–178

Das Dhiman, Sharma Arunima, Rajendran Praveenbalaji, Pramanik Manojit (2021) Another decade of photoacoustic imaging. Phy Med Biol 66:05TR01

Diebold GJ, Sun T, Khan MI (1991) Photoacoustic monopole radiation in one, two, and three dimensions. Phys Rev Lett 67(24):3384

Galanzha Ekaterina I, Zharov Vladimir P (2013) Circulating tumor cell detection and capture by photoacoustic flow cytometry in vivo and ex vivo. Cancers 5(4):1691–1738

Gerald Lim HW, Wortis Michael, Mukhopadhyay Ranjan (2002) Stomatocyte-discocyte-echinocyte sequence of the human red blood cell: evidence for the bilayer-couple hypothesis from membrane mechanics. Proc Natl Acad Sci 99(26):16766–16769

He Li LuLu, Li Xuejin, Buffet Pierre A, Dao Ming, Karniadakis George E, Suresh Subra (2018) Mechanics of diseased red blood cells in human spleen and consequences for hereditary blood disorders. Proc Natl Acad Sci 115(38):9574–9579

https://www.cmu.edu/biolphys/deserno/pdf/sphere_equi.pdfhttps://www.cmu.edu/biolphys/deserno/pdf/sphere_equi.pdf

Ishimaru Akira (2002) Wave propagation and scattering in random media. Wiley, New York

Juratli Mazen A, Menyaev Yulian A, Sarimollaoglu Mustafa, Siegel Eric R, Nedosekin Dmitry A, Suen James Y, Melerzanov Alexander V, Juratli Tareq A, Galanzha Ekaterina I, Zharov Vladimir P (2016) Real-time label-free embolus detection using in vivo photoacoustic flow cytometry. PLoS One 11(5):e0156269

Kaushik Anuj, Saha Ratan K (2021) Characterization of normal and deformed red blood cells using simulated differential photoacoustic cross-section spectral data. J Phys Commun 5:035007

Kaushik Anuj, Sonker Deepak, Saha Ratan K (2019) Study on angular distribution of differential photoacoustic cross-section and its implication in source size determination. J Opt Soc of Am A 36(3):387–396

Kaushik Anuj, Paul Avijit, Saha Ratan K (2020) Systematic analysis of frequency dependent differential photoacoustic cross-section data for source size estimation. J Opt Soc Am A 37(12):1895–1904

Kaushik Anuj, Yalavarthy Phaneendra K, Saha Ratan K (2020) onvergent born series improves the accuracy of numerical solution of time-independent photoacoustic wave equation. J Modern Opt 67(9):849–855

Larkin Timothy J, Kuchel Philip W (2010) Mathematical models of naturally morphed human erythrocytes: stomatocytes and echinocytes. Bull Math Biol 72(6):1323–1333

Morse Philip M, Feshbach Herman (1953) Methods of theoretical physics. McGraw-Hill, New York

Morse Philip M, Uno Ingard K (1968) Theoretical acoustics. McGraw-Hill, New York

Muñoz San Martín S, Sebastián JL, Sancho M, Álvarez G (2006) Modeling normal and altered human erythrocyte shapes by a new parametric equation: application to the calculation of induced transmembrane potentials. Bioelectromagnetics 27(7):521–527

Neukammer Jörg, Gohlke Carsten, Höpe Andreas, Wessel Thomas, Rinneberg Herbert (2003) Angular distribution of light scattered by single biological cells and oriented particle agglomerates. Appl Op 42(31):6388–6397

Ranjan Mukhopadhyay HW, Lim Gerald, Wortis Michael (2002) Echinocyte shapes: bending, stretching, and shear determine spicule shape and spacing. Biophysical J 82(4):1756–1772

Saha Ratan K (2020) Numerical solution to the time-independent inhomogeneous photoacoustic wave equation using the born series methods. J Opt Soc Am A 37(12):1907–1915

Saha Ratan K (2021) Solving time-independent inhomogeneous optoacoustic wave equation numerically with a modified green's function approach. J Acoust Soc Am 149(6):4039–4048

Saha Ratan K, Kolios Michael C (2011) A simulation study on photoacoustic signals from red blood cells. J Acoust Soc Am 129(5):2935–2943

Saha Ratan K, Karmakar Subhajit, Adhikari Arunabha, Kolios Michael C (2017) Photoacoustic field calculation for nonspherical axisymmetric fluid particles. Biomed Phys Eng Express 3(1):015017

Schiff Leonard I (1969) Quantum mechanics. McGraw-Hill Education, Asia

Sharma Subodh K, Saha Ratan K (2009) A new approximate formula for scattering of plane acoustic waves by a spherical obstacle. Acta Acust United Acust 95(1):1–6

Strohm Eric M, Berndl Elizabeth SL, Kolios Michael C (2013a) Probing red blood cell morphology using high-frequency photoacoustics. Biophysical J 105(1):59–67

Strohm Eric M, Berndl Elizabeth SL, Kolios Michael C (2013b) High frequency label-free photoacoustic microscopy of single cells. Photoacoustics 1(3–4):49–53

Wang Lihong V (2017) Photoacoustic imaging and spectroscopy. CRC Press, Boca Raton

Wang Lihong V, Yao Junjie (2016) A practical guide to photoacoustic tomography in the life sciences. Nat Methods 13(8):627

Publisher's Note Springer Nature remains neutral with regard to jurisdictional claims in published maps and institutional affiliations.